Materials & Design 221 (2022) 110913

Contents lists available at ScienceDirect

Materials & Design

journal homepage: www.elsevier.com/locate/matdes

Ultraprecision tool-servo cutting of pure nickel for fabricating micro/nanostructure arrays

Hanheng Du [a], Mengnan Jiang [b], Zhiwei Zhu [c], Zuankai Wang [b,*], Suet To [a,*]

[a] State Key Laboratory of Ultra-precision Machining Technology, Department of Industrial and Systems Engineering, The Hong Kong Polytechnic University, Hong Kong, China
[b] Department of Mechanical Engineering, City University of Hong Kong, China
[c] School of Mechanical Engineering, Nanjing University of Science and Technology, China

HIGHLIGHTS

- The ultraprecision tool-servo cutting process was proposed to generate the micro/nanostructure arrays on pure nickel surfaces.
- The micro-lens array was generated with high fabrication accuracy, demonstrating the effectiveness of the proposed cutting process.
- The sawtooth-shaped nanostructure array on an area of 13 mm × 14 mm was generated with high fabrication efficiency.
- Sawtooth-shaped nanostructure array triggers the generation of structural colors with high chromaticity and high brightness.

GRAPHICAL ABSTRACT

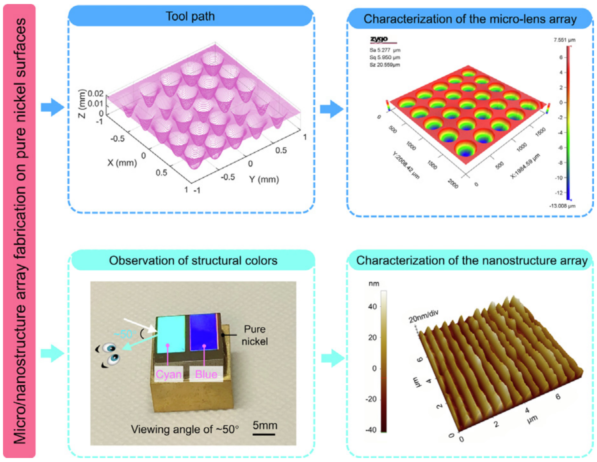

ARTICLE INFO

Article history:
Received 22 May 2022
Revised 25 June 2022
Accepted 29 June 2022
Available online 2 July 2022

Keywords:
Pure nickel
Ultraprecision tool-servo cutting process
Micro-lens array
Sawtooth-shaped nanostructure array
Structural color

ABSTRACT

The fabrication of micro/nanostructure arrays on nickel or nickel alloy surfaces is still a challenge because of the high hardness and low thermal conductivity. Motivated by this, this study proposed the ultraprecision tool-servo cutting process to fabricate micro/nanostructure arrays on the nickel surfaces. Experimental results showed the micro-lens array and sawtooth-shaped nanostructure array were successfully fabricated on pure nickel surfaces. The fabrication error of the micro-lens array is<1.2%, demonstrating the high fabrication accuracy of the proposed cutting process. Furthermore, the sawtooth-shaped nanostructure array triggers the generation of different structural colors. The cyan, blue, yellow, and green with high chromaticity and high brightness were clearly observed on the pure nickel surface. The fabrication time of the sawtooth-shaped nanostructure array is 45 mins, demonstrating the high fabrication efficiency of the proposed cutting process. This study provides a flexible and highly efficient fabrication method to generate micro/nanostructure arrays, which could extend the application fields of nickel and its alloy to optics.

---

* Corresponding authors.
E-mail addresses: zuanwang@cityu.edu.hk (Z. Wang), sandy.to@polyu.edu.hk (S. To).

https://doi.org/10.1016/j.matdes.2022.110913
0264-1275/

1. Introduction

With the fast development of aerospace and other advanced industries, nickel and its alloys have been attracted more and more attention and are extensively used in rocket engines, petrochemical equipment, steam power plants, submarines, gas turbines, nuclear reactors, and other high-temperature applications because of admirable properties, including the excellent mechanical properties, high corrosion resistance, and superior oxidation resistance in extreme high working temperature [1–8]. Nowadays, nickel and nickel alloys are typically produced by casting [9], wrought [10], and direct metal laser sintering [11]. However, as difficult-to-cutting materials, nickel and its alloys face many challenges in cutting due to the high hardness bringing about the high cutting force, the low thermal conductivity bringing about the high cutting temperature, and the high chemical affinity bringing about the rapid tool wear [12–15].

In the past several years, many researchers investigated different cutting processes for nickel and nickel alloys. Turning is the most widely used cutting process to fabricate metal materials. Tan and Zhang [16] analyzed the wear mechanism of the cutting tool using the scanning electron microscope and auger electron spectroscopy when turning the pure nickel. They also investigated the influences of cutting parameters on tool wear. Furushiro et al. [17] found that the tool wear could be dramatically reduced by adding the phosphorous in turning the pure nickel and electroless nickel deposits. The erosion tests and the ab initio molecular dynamics calculations revealed the wear suppression mechanism. Parida and Maity [18] proposed a heat-assisted turning process for the nickel-base alloy and found that the heat-assisted turning increased the tool life and reduced the cutting force and power consumption in comparison with the room temperature machining condition. Milling is another widely used cutting process. Şirin et al. [19] analyzed the influences of the different cutting environments on surface roughness, cutting force, and cutting temperature when milling nickel alloy X-750. They found that the nanofluid-based minimum quantity lubrication improved the surface roughness and decreased the cutting force and cutting temperature. Li et al. [20] investigated the wear patterns and wear mechanisms of the end-milling ceramic tool. They confirmed that the major wear patterns were flank wear and breakage, and the main wear mechanisms were adhesion and diffusion wear. In addition to the turning and milling processes, the grinding was also applied to remove workpiece materials. Guo et al. [21] investigated the effect of the cutting parameters and the wheel wear on the grinding of a nickel alloy. They found that the thermal damage appeared when grinding with a worn wheel. Cao et al. [22] designed an ultrasonic vibration device to realize ultrasonic vibration-assisted grinding (UVAG). Experiments showed that this UVAG process reduced the grinding force and enhanced the machined surface quality of the nickel-based superalloy in comparison with the conventional creep-feed grinding.

Although the turning, milling, and grinding processes have been employed to study the tool wear, cutting forces, cutting parameters, and surface quality, the generation of micro/nanostructure arrays on nickel or nickel alloy was rarely reported in the literature. Laser ablation is a common method to fabricate micro/nanostructure arrays on workpiece surfaces [2324], but the dimensional accuracy and surface quality are difficult to guarantee. With the advancement of cutting technologies, ultraprecision cutting processes have fast developed for the machining of micro/nanostructure arrays with high surface quality on the workpiece surfaces, such as the ultraprecision fly cutting process [2526] and ultraprecision tool-servo cutting process [27]. In the ultraprecision fly cutting process, the diamond cutting tool rotates with the spindle to intermittently remove the workpiece materials. Although it has the high flexibility of fabricating micro/nanostructure arrays with nanometric surface roughness and low form error, the extremely low fabrication efficiency limits mass production [2829]. The ultraprecision tool-servo cutting process is attracting ever-increasing attention since it provides a highly efficient and highly flexible fabrication method for the micro/nanostructure arrays. In the ultraprecision tool-servo cutting process, if the tool-servo responds slowly, it is called slow-tool-servo cutting. If the tool-servo responds fast, it is called the fast-tool-servo cutting. Yi and Li [30] demonstrated a tool trajectory strategy of the slow-tool-servo cutting, in which the entire micro-lens array with optical quality and finish was fabricated in a single operation. Over the scan length of 0.7 mm, the surface roughness R_a was 34.5 nm. For the fast-tool-servo cutting, Zhu et al. [31] used this process to machine a micro-freeform lens array. Yuan et al. [32] proposed the surface generation algorithm of the fast-tool-servo cutting. The hierarchical sinusoidal surfaces were machined and their influence on the wettability was investigated. However, most of the current research works on the ultraprecision tool-servo cutting pay much attention to the fabrication of micro/nanostructure arrays on the easy-to-cutting material surfaces, such as copper or aluminum. Little systematic work has been reported about the generation of micro/nanostructure arrays on the nickel or nickel alloy surfaces.

In this study, the systematic exploration of the fabrication of micro/nanostructure arrays on the pure nickel surfaces is investigated for the first time using the ultraprecision tool-servo cutting process. The working principles of the ultraprecision tool-servo cutting process are illustrated in Section 2. The micro-lens array and sawtooth-shaped nanostructure array are fabricated on the pure nickel surfaces. And after the fabrication experiments, detailed discussions on the topographies of micro/nanostructure arrays, cutting forces, and tool wear are given in Section 4, followed by the conclusions in Section 5.

2. Ultraprecision tool-servo cutting

In the ultraprecision tool-servo cutting process, the slow-tool-servo cutting has a longer stroke, which is suited for the fabrication of microstructure arrays with large sag. Fast-tool-servo cutting can offer higher working frequency with an extra attachment, which is appropriate for the fabrication of nanostructures with high fabrication efficiency. Both can provide a good surface finish and high form accuracy without any additional post-processing.

2.1. Slow-tool-servo cutting

In the slow-tool-servo cutting, a natural single-crystal diamond (SCD) cutting tool is stationed on the Z-axis of the ultraprecision lathe and oscillates together with this axis at a low working frequency, typically<200 Hz. The workpiece is installed on the spindle (also called C-axis), which is controlled in position mode. The hardware configuration of the slow-tool-servo cutting is shown in Fig. 1. In the slow-tool-servo cutting, motions of all axes are fully synchronized and controlled to machine the microstructure arrays. The SCD cutting tool oscillates forward and backward on the workpiece surface along the Z-axis. It also synchronizes with the angular position of the C-axis and the translational position of the X-axis [33]. In other words, the Z-axis coordinate of the SCD cutting tool is a function of the C-axis coordinate and X-axis coordinate. When machining a microstructure array, all microstructures are continuously fabricated in one turning cycle [34]. The slow-tool-servo cutting has the merits of longer stroke, easy control, and simpler setup, which enables it to machine microstructure arrays on the workpiece surface.

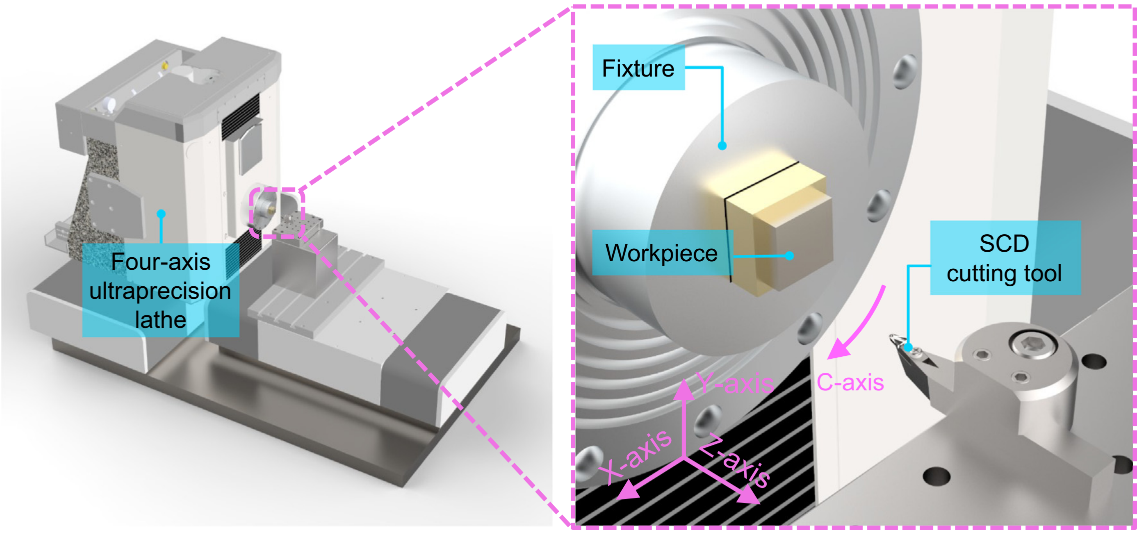

Fig. 1. Hardware configuration of the slow-tool-servo cutting.

Micro-lens array, as a typical microstructure array, has received even-increasing attention due to its superior performance in imaging [35–37], illumination [38–40], and beam shaping [41–43]. Therefore, the micro-lens array is chosen as the target to be fabricated on a micrometer scale in this study. The geometrical characteristics of the desired micro-lens array are shown in Fig. 2 (a). Each micro-lens has a concave spherical surface, and its curvature radius (r) is 0.8 mm. Other dimensions of characteristics are listed in Table 1. These micro-lenses are evenly distributed in the X-axis and Y-axis directions.

The tool path of this micro-lens array can be created using a computer-aided manufacturing software "DIFFSYS" (Precitech, UK), which is described in the form of cylindrical coordinates (C, X, Z). The discrete points are computed at a constant angular step of 0.5° around the C-axis. The discrete points (C, X, Z) can be converted to the Cartesian coordinate (x, y, z) by Eq. (1).

$$\begin{cases} x = X\cos(C) \\ y = X\sin(C) \\ z = Z \end{cases} \tag{1}$$

Fig. 2(b) shows the tool path of the 5 × 5 micro-lens array in the Cartesian coordinate system. The feedrate was herein set as 10 μm/rev to have a much clearer view, which was five times larger than the value of the practical feedrate in fabrication experiments.

Table 1
Geometrical dimensions of the 5 × 5 micro-lens array.

Dimension	S_x	S_y	l	d	r
Value (mm)	0.3826	0.3826	0.3326	0.0175	0.8

2.2. Fast-tool-servo cutting

The fast-tool-servo cutting can fabricate non-rotationally symmetric nanostructure arrays [44]. The additional attachment for the tool drive in the fast-tool-servo cutting is called the vibration generator, which is commonly piezoelectrically driven with high bandwidth and high stiffness [45]. Fig. 3 shows the hardware configuration of the fast-tool-servo cutting, in which the ultraprecision lathe provides the linear motions along the directions of X-, Y-, and Z-axes, and the two-degree-of-freedom vibration generator (2DOF-VG) provides the periodic vibration trajectory. An SCD cutting tool with a sharp cutting edge is utilized as the cutting tool. In addition to the above hardware, it also needs a 2DOF-VG driving system, which consists of a computer, a multifunction I/O device, and a piezo amplifier. As a core component of fast-tool-servo cutting, the 2DOF-VG plays an important role in fabricating the nanostructure array. A novel 2DOF-VG was developed in our previous work [46]. Through the sweeping frequency test, it is found that the

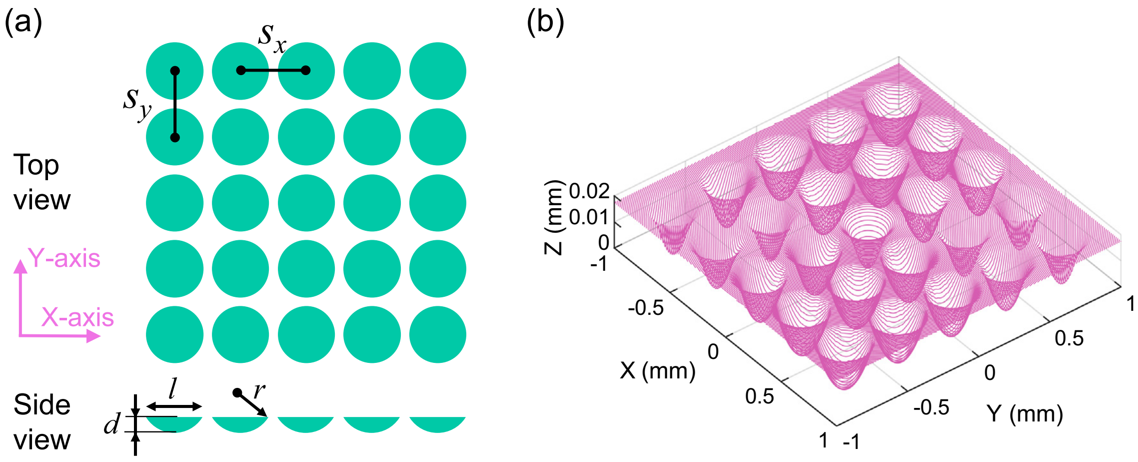

Fig. 2. (a) Geometrical characteristics and (b) tool path of the designed 5 × 5 micro-lens array.

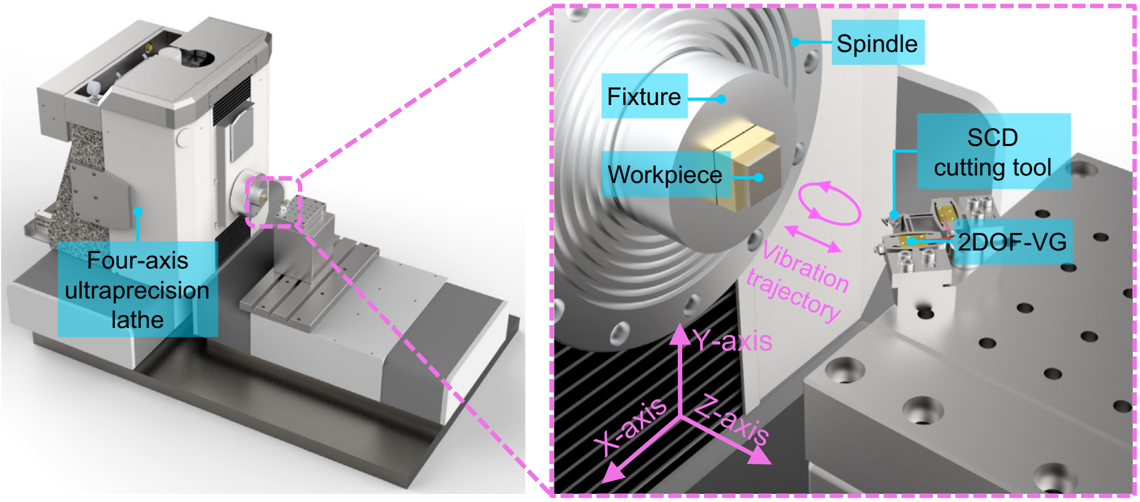

Fig. 3. Hardware configuration of the fast-tool-servo cutting.

working frequency of the developed 2DOF-VG can be up to 3000 Hz.

In the fast-tool-servo cutting, the cutting tool will remove the workpiece material using its rake face and cutting edge, and fabricate the nanostructure array along the tool path, as illustrated in Fig. 4. Without loss of generality, the tool path is mathematically expressed as:

$$x_{FTS}(t) = d^{x}_{FTS}(t) + V_{FTS}t \tag{2}$$

$$z_{FTS}(t) = d^{z}_{FTS}(t) \tag{3}$$

where $d^{x}_{FTS}(t)$ and $d^{z}_{FTS}(t)$ are the vibration trajectories in the X-axis and Z-axis directions, which are provided by the 2DOF-VG. Generally, $d^{x}_{FTS}(t)$ and $d^{z}_{FTS}(t)$ are sinusoidal functions. V_{FTS} is the nominal cutting velocity provided by the ultraprecision lathe. According to Eqs. (2) and (3), the tool path ($x_{FTS}(t)$, $z_{FTS}(t)$) can be flexibly created to fabricate various nanostructure arrays on the workpiece surface.

Besides, the nanostructure array with regular facet spacing (S_n) have an optical effect and can induce the generation of different colors on the workpiece surface, which will be in-detailed presented in the results and discussion section.

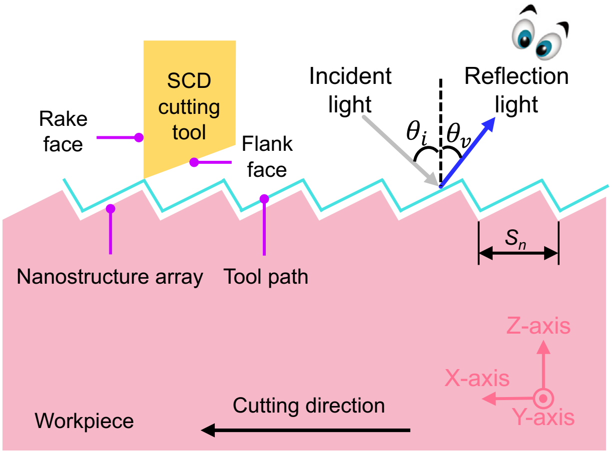

Fig. 4. Fabrication principle of the nanostructure array.

3. Experimental procedure

The fabrication experiments of micro/nanostructure arrays on the pure nickel surfaces were performed on an ultraprecision lathe (350FG, Moore Nanotechnology) with four axes. This lathe has three linear axes with a 0.034 nm feedback resolution. For the rotational axis (spindle), the maximum rotational speed in the positioning mode can be 3000 rpm with a feedback resolution of 0.07 arc seconds. So, this lathe can provide ultraprecision control for the tool-servo cutting process to fabricate the micro/nanostructure arrays. Fig. 5 (a) shows the experimental setup of the slow-tool-servo cutting. The pure nickel cube (Keple Technology Co., Ltd., China) with dimensions of 15 × 15 × 5 mm^3 was glued into a fixture, which was sucked on the spindle. The chemical composition of the pure nickel is listed in Table 2. An SCD cutting tool (N0.50mLECi, Contour Fine Tooling Inc.) was used to fabricate the micro-lens arrays on the workpiece surface. This cutting tool was stationed on the dynamometer via a screw. Specifications of the cutting tool are summarized in Table 3. A high-pressure oil mist was used via a nozzle to reduce the heat at the tool-workpiece interface. Fig. 5 (b) shows the experimental setup of the fast-tool-servo cutting. The workpiece was also fixed via a fixture. The 2DOF-VG was mounted on a dynamometer via a screw. The detailed specifications of the SCD cutting tool (N0.50mLEixCV1503, Contour Fine Tooling Inc.) in the fast-tool-servo cutting are also listed in Table 3. During the nanostructure array fabrication, the computer provided command signals. A multifunction I/O device converted these digital signals into analog signals. The piezo amplifiers were employed to magnify analog signals, which were inputted into the piezoelectric actuators (PK4FA2H3P2, Thorlabs Inc.) to drive the 2DOF-VG. And the corresponding cutting parameters for fabricating the nanostructure array are listed in Table 3.

For obtaining a planer surface with high surface quality, the original surface of the workpiece before the ultraprecision tool-servo cutting was turned using the depth-of-cutting of 3 μm, the spindle speed of 1500 rpm, and the feedrate of 4 mm/min. Besides, the cutting forces during fabricating micro/nanostructure arrays were measured through the cutting force measurement system, which contains a dynamometer (9256C1, Kistler Instrument Corp.) and a charge amplifier (5080, Kistler Multichannel Charge amplifier) [47]. The sampling rate of capturing cutting force data was 60 kHz for sufficiently collecting the cutting forces. After the experiments, all workpieces were cleaned for 5 mins using an ultrasonic cleaner.

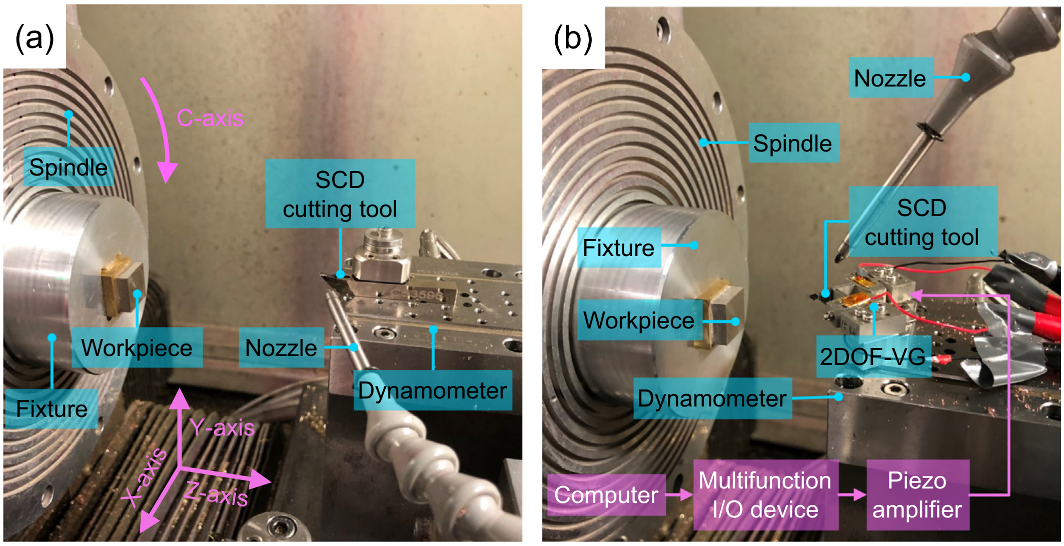

Fig. 5. Experiment setup of (a) slow-tool-servo cutting and (b) fast-tool-servo cutting.

Table 2
Chemical composition of the pure nickel.

Composition	Ni + Co	Cu	Si	Mn	C	Mg	Zn	Cd	S
Weight, %	>99.5	0.012	0.01	<0.01	0.004	<0.005	<0.005	<0.002	<0.001
Composition	P	Fe	Pb	Bi	As	Sb	Sn	Others	
Weight, %	<0.001	0.01	<0.002	<0.002	<0.002	<0.002	<0.002	<0.5	

Table 3
Tool geometry and cutting parameters.

Slow-tool-servo cutting				Fast-tool-servo cutting			
Tool nose radius (mm)	0.478	Constant angle	0.5°	Tool nose radius (mm)	0.480	Depth-of-cutting (μm)	4
Tool rake angle	0°	Depth-of-cutting (μm)	2	Tool rake angle	0°	Frequency (Hz)	1000
Tool flank angle	15°	Feedrate (mm/min)	0.248	Tool flank angle	15°	Phase difference	0°
				V_{FTS}(mm/min)	41.46 (Region A)	Voltage (V)	40
					36.75 (Region B)		

4. Results and discussion

4.1. Characterization of the microstructure array

Before fabricating the micro-lens array, a mirror surface with a 4 nm surface roughness was firstly obtained, as presented in Fig. 6 (a). The slow-tool-servo cutting was conducted to fabricate the 5 × 5 micro-lens array, which was in the center of the workpiece surface. An optical microscope (BX60, Olympus Corp.) was employed to have a much clearer observation, as shown in Fig. 6 (b). The 25 micro-lenses were successfully fabricated on the pure nickel surface.

Further, the three-dimensional topography of the micro-lens array was obtained by a white light interferometer (Nexview^{TM}, Zygo Corp.), as shown in Fig. 7 (a). Each micro-lens shares the same characteristics of the three-dimensional topography, which indicates that the uniform quality of the array was well achieved. To quantify the form accuracy of the fabricated micro-lens array, a cross-sectional profile passing through the center of micro-lenses was extracted and plotted in Fig. 7 (b).

Each micro-lens has almost the same length (l) and depth (d) in the whole fabrication region. The average value of the measured l and measured d are 336.0 μm and 17.7 μm, respectively. Take the designed dimensions as "true", the corresponding fabrication errors are 1.02% and 1.14%, demonstrating the high fabrication accuracy of the proposed process. Fig. 8 shows the three-dimensional topography of a micro-lens and surface roughness of four 100 μm × 100 μm regions. The concave spherical surface without any bur was obtained and the average value of the surface roughness of four different regions is 0.005 μm, showing the high surface finish of the micro-lens array.

4.2. Characterization of the nanostructure array

After obtaining the mirror surface, the sinusoidal signal with the frequency of 1000 Hz was used to induce the 2DOF-VG to produce the line-shaped vibration trajectory in the Z-axis direction, as depicted in Fig. 4. Two regions, named region A and region B, were fabricated using different nominal cutting velocities. The nominal cutting velocities in the X-axis direction were 41.46 mm/min for region A and 36.75 mm/min for region B, respectively. The feed in the Y-axis direction was 70 μm for both regions, and other cutting parameters are listed in Table 3. When finishing one cutting motion on X-axis, the cutting tool would return to the origin point and then moves a feed in the Y-axis direction. The cycle starts until finishing all fabrication.

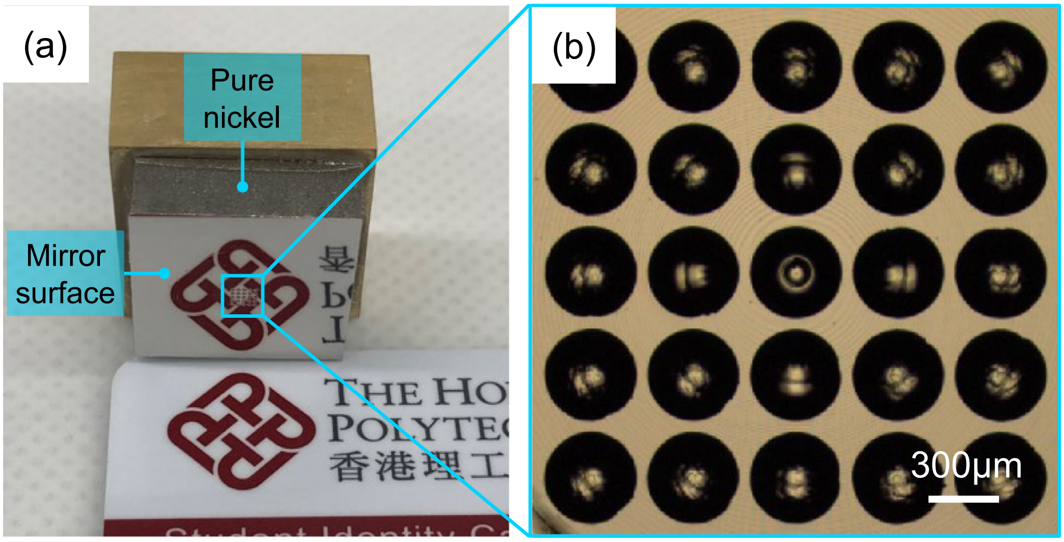

Fig. 6. (a) Photograph and (b) microscope image of the micro-lens array.

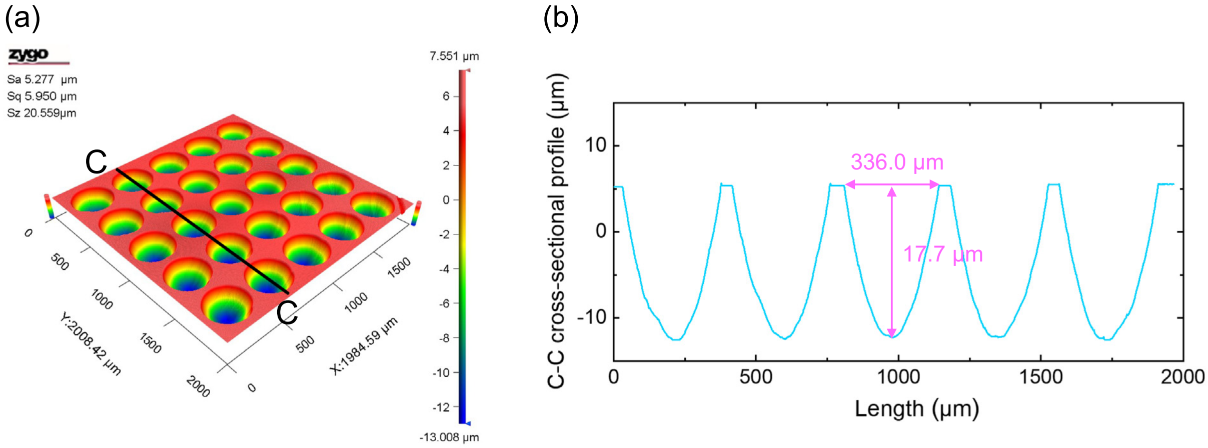

Fig. 7. (a) Three-dimensional topography of the micro-lens array and (b) cross-sectional profile.

Fig. 9 shows the various structural colors generated on the pure nickel surface, which were visible to the naked eye. When the viewing angle is ~ 50°, region A and region B show the cyan and blue under natural light. When the viewing angle is ~ 60°, they display the yellow and green under natural light. Similar to easy-to-cutting metal materials, such as copper [48] and aluminum [49], it can be found that bright structural colors can be generated on the pure nickel surface. The total fabrication time for region A and region B is about 45 min, which demonstrates that fast-tool-servo cutting is a very highly efficient fabrication method. The generated structural colors also make the nickel possess optical performance and extend the application fields of the nickel to optics.

To estimate the purity of the structural colors, the chromaticity coordinates (x,y) are measured three times by a chroma meter (CS-200, Konica Minolta, Inc.), and then are plotted on the CIE 1931 chromaticity diagram, as illustrated in Fig. 10. The chromaticity coordinate for each structural color locates very closely, which demonstrates that each structural color has great color purity. It also indicates the proposed cutting process can produce intense structural colors. To quantify the difference between the chromaticity coordinates of the single-color, the mean and mean squared error (MSE) were calculated and listed in Table 4. It can be found that the maximum MSE occurs in the chromaticity y-coordinate of the green color, but its value is also only 0.0172, which further proves that the structural colors that were generated by the proposed cutting process have high purity.

To investigate the generation mechanism of structural colors, an atomic force microscope (AFM) (Park XE-70, Park Systems, Corp.) was used to characterize the nanostructure array in region A and region B. Their three-dimensional topographies are shown in Fig. 11 (a) and Fig. 12 (a). It is found that the periodic nanostructure array was fabricated on the pure nickel surface. Fig. 11 (b) and Fig. 12 (b) show the cross-sectional profiles along the AA line and BB line, which demonstrate that the nanostructure array has the sawtooth-shaped profile. The AFM data were further analyzed by the software XEI (Park Systems, Corp.) to detect the topographical distribution and surface homogeneity using the histogram and power spectral density (PSD). Fig. 11 (c) and Fig. 12 (c) show the height distribution histograms of the nanostructure array. The negative value of the height presents the valley of the three-dimensional topography. The positive value of the height presents the peak of the three-dimensional topography. It can be found the distribution is left–right symmetrical and the symmetrical center is 0 nm, which demonstrates the high homogeneity of height distribution for the whole measurement region. A quantitative analysis of facet spacing (S_n) between two adjacent nanostructures for

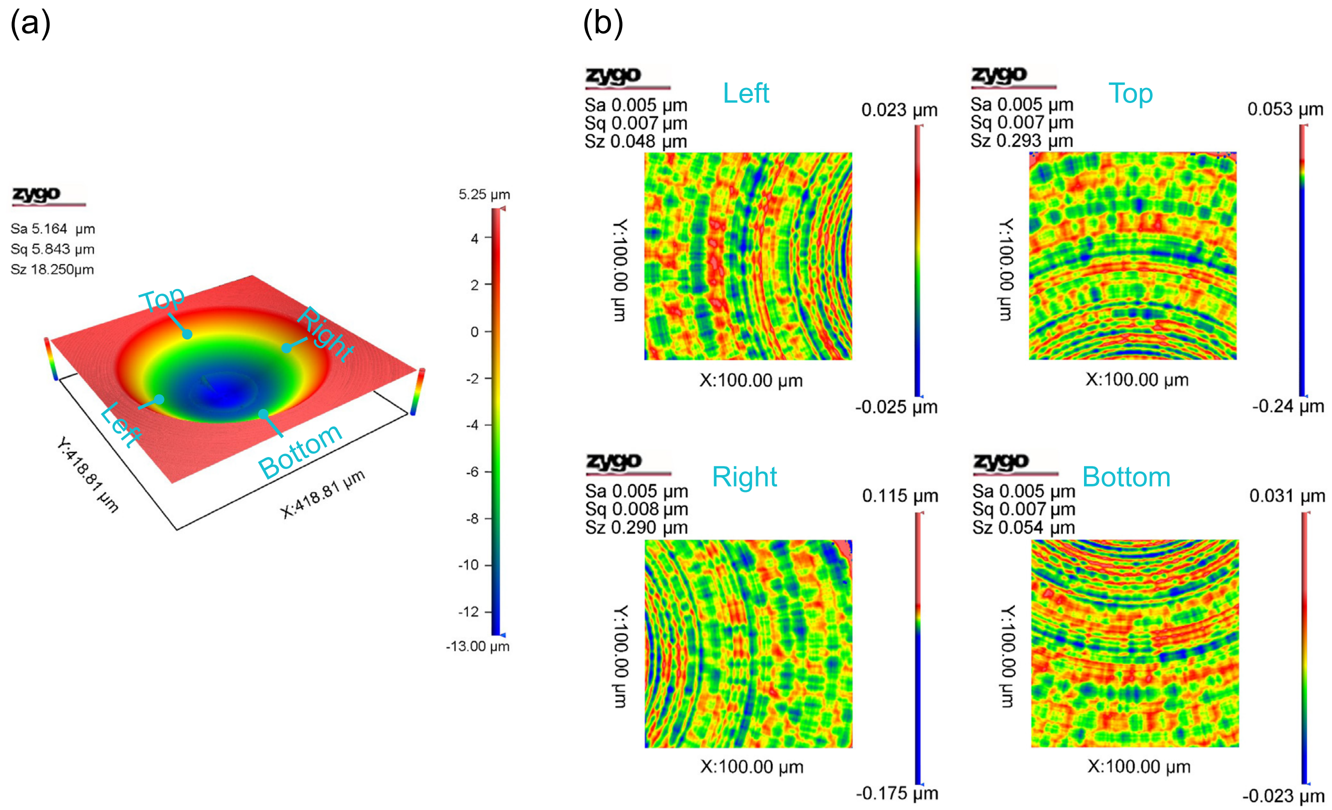

Fig. 8. Three-dimensional topography of a micro-lens and surface roughness regarding four different regions.

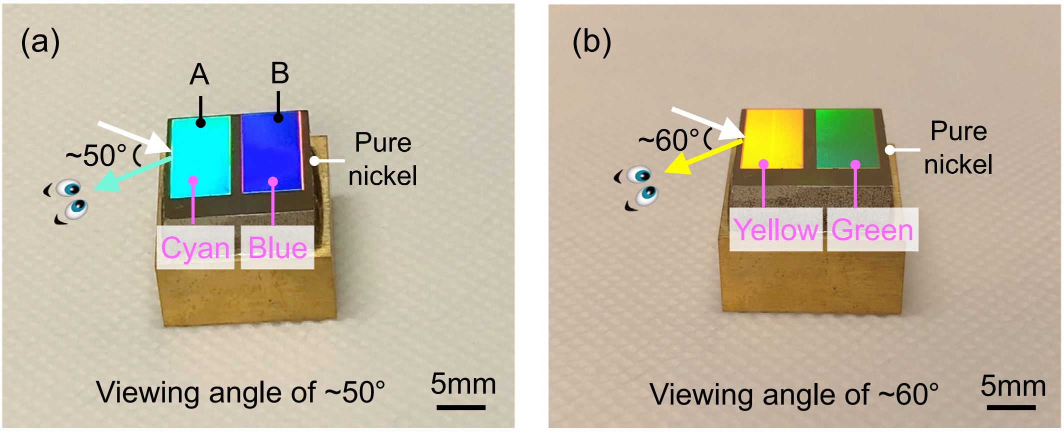

Fig. 9. Photographs of the different structural colors.

the whole measurement region is conducted by the PSD graphs, as shown in Fig. 11 (d) and Fig. 12 (d). The reciprocal of the spatial frequency regarding peak represents the average S_n. They are 693.9 nm and 613.0 nm for region A and region B, which correspond well with the theoretical values (691.0 nm and 612.5 nm). It further demonstrates the high fabrication accuracy of the proposed process.

In essence, the physical interaction between the sawtooth-shaped nanostructure array and the visible light triggers the generation of the structural colors, which can be mathematically expressed by the grating equation [5051]:

$$sin\theta_i + sin\theta_v = m\lambda_n/S_n(m = 0, \pm 1, \cdots) \tag{4}$$

where θ_i and θ_v are the incident angle and viewing angle, as shown in Fig. 4. m is the reflection order. λ_n is the wavelength of the reflection light. The natural light was used as the incident light (θ_i = 0°) and the reflection order m was assumed to be 1 in this study. The grating equation can be simplified to:

$$\lambda_n = S_n sin\theta_v \tag{5}$$

Therefore, a certain structural color (λ_n) can be viewed at the corresponding viewing angle (θ_v) when the facet spacing (S_n) of the nanostructure array is constant.

4.3. Cutting force analysis

Cutting force is a significant indicator to reflect the features of the cutting process. Fig. 13 shows the measured cutting forces of the slow-tool-servo cutting and fast-tool-servo cutting along the depth-of-cutting direction. They also correspond to the Z-axis

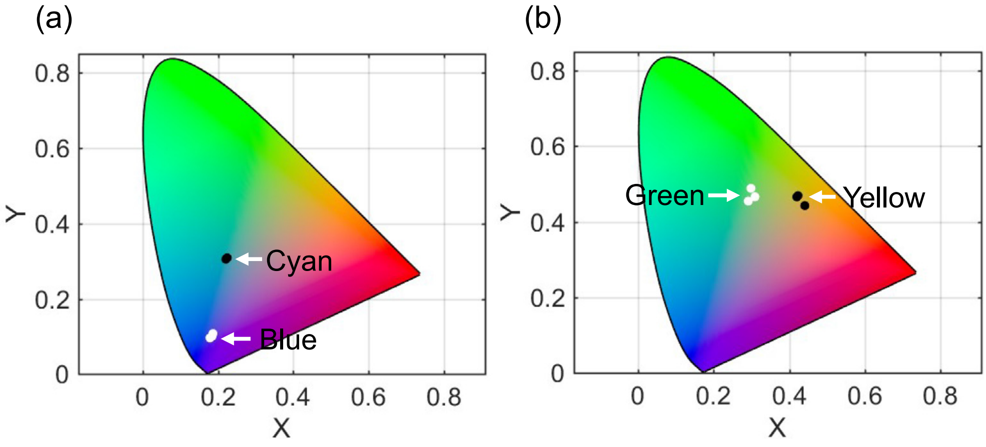

Fig. 10. Chromaticity coordinates of different structural colors on the CIE 1931 chromaticity diagram.

Table 4
Mean and MSE of chromaticity coordinates of different structural colors.

	Chromaticity *x*-coordinate		Chromaticity *y*-coordinate	
	Mean	MSE	Mean	MSE
Cyan	0.2227	0.0018	0.3069	0.0019
Blue	0.1833	0.0040	0.1014	0.0058
Yellow	0.4282	0.0114	0.4593	0.0143
Green	0.3000	0.0089	0.4699	0.0172

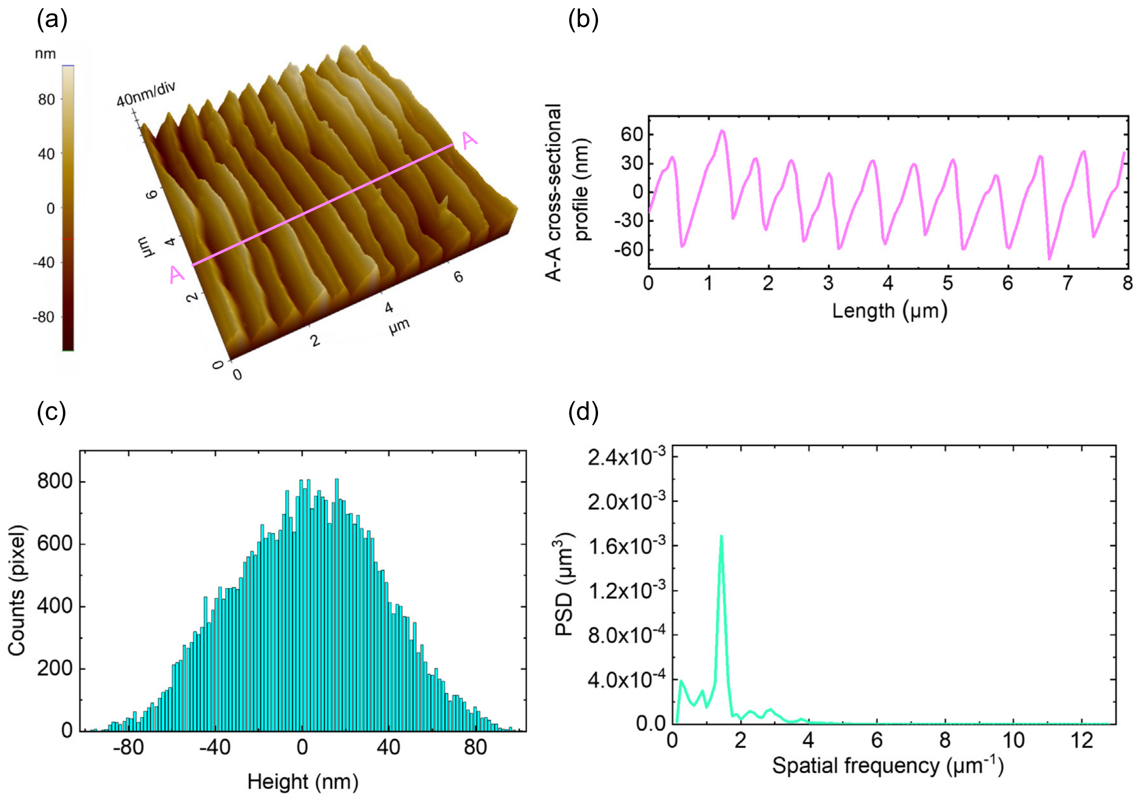

Fig. 11. (a) AFM map of the nanostructure array in region A, (b) cross-sectional profile, (c) height distribution histogram of the nanostructure array, and (d) PSD graph of the facet spacing of the nanostructure array.

direction, as shown in Fig. 5. It is observed that the cutting forces periodically change with time. It is mainly because no matter what it is the micro-lens array fabrication or the sawtooth-shaped nanostructure array fabrication, the corresponding tool path is periodic, as illustrated in Fig. 2 and Fig. 4. Therefore, the cutting forces periodically increase and decrease with the periodic tool

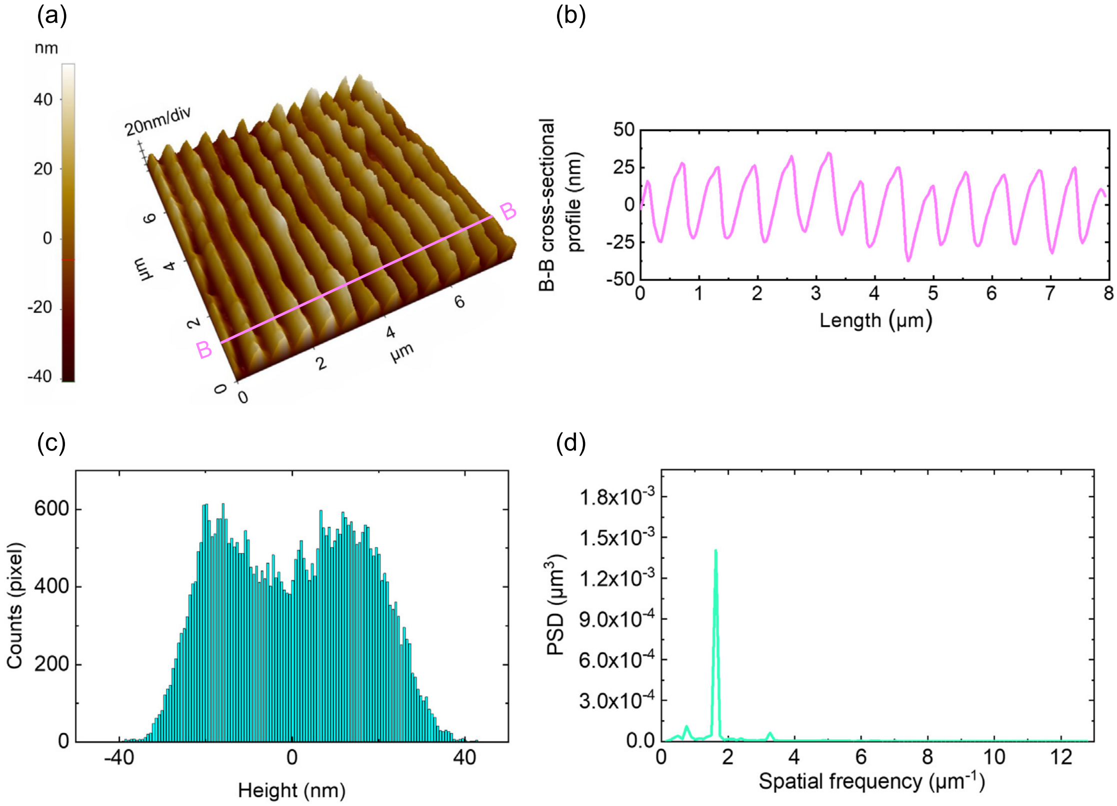

Fig. 12. (a) AFM map of the nanostructure array in region B, (b) cross-sectional profile, (c) height distribution histogram of the nanostructure array, and (d) PSD graph of the facet spacing of the nanostructure array.

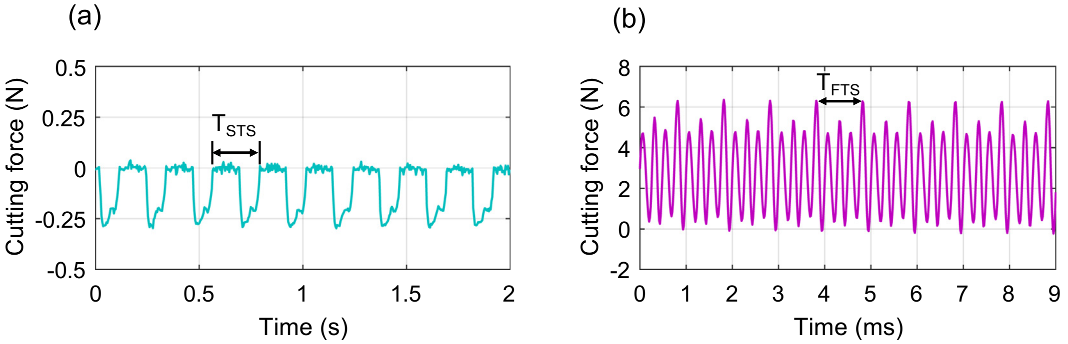

Fig. 13. Measured cutting forces of (a) slow-tool-servo cutting and (b) fast-tool-servo cutting.

path. The period (T_{STS}) in the slow-tool-servo cutting is 0.228 s, and it reduces with the decrease of the spiral radius of the tool path. The period (T_{FTS}) in the fast-tool-servo cutting is 1 microsecond. It is the reciprocal of the frequency (1000 Hz) and keeps unchanged, which also demonstrates the difference between the slow-tool-servo cutting and the fast-tool-servo cutting.

For the cutting forces of the slow-tool-servo cutting plotted in Fig. 13 (a), the average peak-to-valley value is 0.28 N. For the fast-tool-servo cutting plotted in Fig. 13 (b), the average peak-to-valley value is 6.38 N. It can be found the average peak-to-valley value of the slow-tool-servo cutting is smaller than that of the fast-tool-servo cutting, which is caused by the different depth-of-cutting. The larger the depth-of-cutting, the larger the cutting force. In the fabrication of the sawtooth-shaped nanostructure array, the fast-tool-servo cutting sets a larger depth-of-cutting.

4.4. Cutting tool observation

The proper cutting process can efficiently reduce tool wear. After fabricating micro/nanostructure arrays, the SCD cutting tools were detected using a scanning electron microscope (SEM) (Hitachi Electron Microscope TM3000), as presented in Fig. 14. By observing the rake face and the cutting edge, no obvious tool wear was found after the proposed ultraprecision tool-servo cutting process. In the fabrication of micro/nanostructure arrays, the cutting tool intermittently contacts the workpiece surfaces, which helps the cutting tool to be cooled and lubricated effectively. Consequently, the tool wear can be significantly reduced, which also demonstrates that the ultraprecision tool-servo cutting process is very suitable for fabricating micro/nanostructure arrays on pure nickel surfaces.

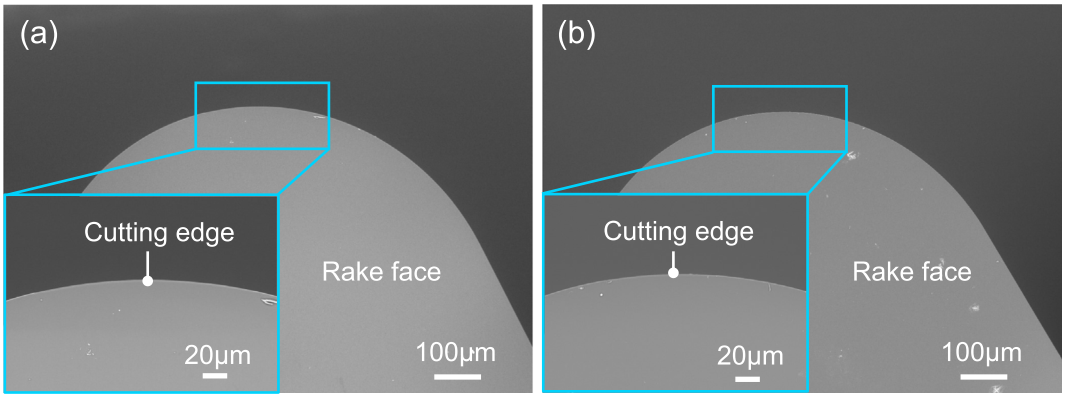

Fig. 14. SEM images of the SCD cutting tools after (a) slow-tool-servo cutting and (b) fast-tool-servo cutting.

5. Conclusions

In this work, the ultraprecision tool-servo cutting process was proposed to fabricate micro/nanostructure arrays on pure nickel surfaces with high fabrication accuracy and high fabrication efficiency. In this cutting process, the slow-tool-servo cutting was employed to fabricate the microstructure array, and the fast-tool-servo cutting was employed to fabricate the nanostructure array. A systematic study on the micro/nanostructure array generation, cutting force analysis, and cutting tool observation was carried out. The main conclusions have been drawn:

(1). The 5 × 5 micro-lens array with a high surface finish was fabricated. Compared with the design dimensions, the fabrication error about the length and depth of the micro-lens is only 1.02% and 1.14%, demonstrating the high fabrication accuracy of the proposed cutting process. The corresponding fabrication principle is also in-detailed illustrated.

(2). The sawtooth-shaped nanostructure array was fabricated on an area of 13 mm × 14 mm. The fabrication time is only 45 min, demonstrating the high fabrication efficiency of the proposed cutting process. In addition, this nanostructure array also induces the generation of different structural colors on the pure nickel surface. The cyan, blue, yellow, and green colors were observed, which are triggered by the physical interaction between the sawtooth-shaped nanostructure array and the visible light. The analysis of chromaticity coordinates on the CIE 1931 chromaticity diagram illustrates that these structural colors possess high chromaticity and high brightness.

(3). Cutting forces have periodic changes during the micro/-nanostructure array fabrication. The regular tool path leads to this phenomenon. Besides, no tool wear was found, further verifying that the proposed cutting process is suitable for fabricating micro/nanostructure arrays on pure nickel surfaces.

This study provides an effective and flexible cutting process for generating micro/nanostructure arrays on pure nickel surfaces. It expands the application range of nickel to optics and will help the researchers to study more functional properties of this material.

Data availability

The data that support the findings of this study are available from the first author (Hanheng Du) upon reasonable request.

Declaration of Competing Interest

The authors declare that they have no known competing financial interests or personal relationships that could have appeared to influence the work reported in this paper.

Acknowledgements

This work was supported by the Research Committee of The Hong Kong Polytechnic University (No. G-RK2V), the National Natural Science Foundation of China (No. U19A20104), and Shenzhen Natural Science Foundation (Basic Research Project) (JCYJ20210324131214039).

References

[1] M. Gong, W. Zhou, M.C. Tsai, J. Zhou, M. Guan, M.C. Lin, B. Zhang, Y. Hu, D.Y. Wang, J. Yang, S.J. Pennycook, B.J. Hwang, H. Dai, Nanoscale nickel oxide/nickel heterostructures for active hydrogen evolution electrocatalysis, Nat. Commun. 5 (2014) 1–6, https://doi.org/10.1038/ncomms5695.

[2] D. Popli, M. Gupta, Experimental investigation of tool wear and machining rate in rotary ultrasonic machining of nickel alloy, Mach. Sci. Technol. 22 (3) (2018) 427–453, https://doi.org/10.1080/10910344.2017.1365896.

[3] D. Ulutan, T. Ozel, Machining induced surface integrity in titanium and nickel alloys: A review, Int. J. Mach. Tools Manuf. 51 (3) (2011) 250–280, https://doi.org/10.1016/j.ijmachtools.2010.11.003.

[4] Z. Wang, C. Carrière, A. Seyeux, S. Zanna, D. Mercier, P. Marcus, XPS and ToF-SIMS Investigation of Native Oxides and Passive Films Formed on Nickel Alloys Containing Chromium and Molybdenum, J. Electrochem. Soc. 168 (4) (2021) 041503, https://doi.org/10.1149/1945-7111/abf308.

[5] P. Moghimian, T. Poirié, M. Habibnejad-Korayem, J.A. Zavala, J. Kroeger, F. Marion, F. Larouche, Metal powders in additive manufacturing: A review on reusability and recyclability of common titanium, nickel and aluminum alloys, Addit. Manuf. 43 (2021) 102017.

[6] J. Zhang, P.A. Korzhavyi, J. He, First-principles modeling of solute effects on thermal properties of nickel alloys, Mater. Today Commun. 28 (2021) 102551.

[7] Y. Wang, M. Lu, Z.i. Wang, J. Liu, L. Xu, Z. Qin, Z. Wang, B. Wang, F. Liu, J. Wang, The learning of the precipitates morphological parameters from the composition of nickel-based superalloys, Mater. Des. 206 (2021) 109747.

[8] Z.A. Sentyurina, F.A. Baskov, P.A. Loginov, Y.Y. Kaplanskii, A.V. Mishukov, I.A. Logachev, M.Y. Bychkova, E.A. Levashov, A.I. Logacheva, The effect of hot isostatic pressing and heat treatment on the microstructure and properties of EP741NP nickel alloy manufactured by laser powder bed fusion, Addit. Manuf. 37 (2021) 101629.

[9] A.S. Hakeem, F. Patel, N. Minhas, A. Malkawi, Z. Aleid, M.A. Ehsan, H. Sharrofna, A. Al Ghanim, Comparative evaluation of thermal and mechanical properties of nickel alloy 718 prepared using selective laser melting, spark plasma sintering, and casting methods, J. Mater. Res. Technol. 12 (2021) 870–881. https://doi.org/10.1016/J.JMRT.2021.03.043.

[10] J. Nguejio, F. Szmytka, S. Hallais, A. Tanguy, S. Nardone, M. Godino Martinez, Comparison of microstructure features and mechanical properties for additive manufactured and wrought nickel alloys 625, Mater. Sci. Eng. A. 764 (2019) 138214.

[11] R. Rajesh, M.V. Kulkarni, B.R. Vergis, P. Sampathkumaran, S. Seetharamu, Copper nickel alloys made using direct metal laser sintering method for assessing corrosion resistance properties, Mater. Today Proc. 49 (2022) 703–713, https://doi.org/10.1016/J.MATPR.2021.05.178.

[12] E.O. Ezugwu, Z.M. Wang, A.R. Machado, The machinability of nickel-based alloys: a review, J. Mater. Process. Technol. 86 (1-3) (1999) 1–16, https://doi.org/10.1016/S0924-0136(98)00314-8.

[13] A. Romero, G. Herranz, A.L. Morales, Study of magnetoelastic properties of pure nickel parts produced by metal injection moulding, Mater. Des. 88 (2015) 438–445, https://doi.org/10.1016/J.MATDES.2015.08.137.

[14] D. Xu, Z. Liao, D. Axinte, J.A. Sarasua, R. M'Saoubi, A. Wretland, Investigation of surface integrity in laser-assisted machining of nickel based superalloy, Mater. Des. 194 (2020) 108851.

[15] C. Liu, M. Wan, W. Zhang, Y. Yang, Chip Formation Mechanism of Inconel 718: A Review of Models and Approaches, Chinese J. Mech. Eng. (English Ed. 34 (1) (2021), https://doi.org/10.1186/s10033-021-00552-9.

[16] M.T. Tan, Y.Z. Zhang, Groove Wear of Tools in NC Turning of Pure Nickel, CIRP Ann. 35 (1) (1986) 71–74, https://doi.org/10.1016/S0007-8506(07)61841-1.

[17] N. Furushiro, H. Tanaka, M. Higuchi, T. Yamaguchi, S. Shimada, Suppression mechanism of tool wear by phosphorous addition in diamond turning of electroless nickel deposits, CIRP Ann. 59 (1) (2010) 105–108.

[18] A.K. Parida, K. Maity, Study of machinability in heat-assisted machining of nickel-base alloy, Measurement 170 (2021) 108682.

[19] Ş. Şirin, M. Sarıkaya, Ç.V. Yıldırım, T. Kıvak, Machinability performance of nickel alloy X-750 with SiAlON ceramic cutting tool under dry, MQL and hBN mixed nanofluid-MQL, Tribol. Int. 153 (2021) 106673.

[20] Y. Li, B. Zou, Z. Shi, C. Huang, L. Li, H. Liu, H. Zhu, P. Yao, J. Liu, Wear patterns and mechanisms of sialon ceramic end-milling tool during high speed machining of nickel-based superalloy, Ceram. Int. 47 (4) (2021) 5690–5698.

[21] C. Guo, Z. Shi, H. Attia, D. McIntosh, Power and Wheel Wear for Grinding Nickel Alloy with Plated CBN Wheels, CIRP Ann. 56 (1) (2007) 343–346.

[22] Y. Cao, Y. Zhu, W. Ding, Y. Qiu, L. Wang, J. Xu, Vibration coupling effects and machining behavior of ultrasonic vibration plate device for creep-feed grinding of Inconel 718 nickel-based superalloy, Chinese J. Aeronaut. 35 (2) (2022) 332–345.

[23] Z. Zhang, Q. Zhang, Q. Wang, Y. Fu, J. Xu, Surface microstructuring of single crystalline diamond based on the accumulated energy homogenization in the nanosecond pulsed laser ablation, Opt. Laser Technol. 138 (2021) 106839.

[24] X. Chen, X. Li, P. Zuo, MiSheng Liang, X. Li, C. Xu, Y. Yuan, S. Wang, Three-Dimensional Maskless Fabrication of Bionic Unidirectional Liquid Spreading Surfaces Using a Phase Spatially Shaped Femtosecond Laser, ACS Appl. Mater. & Interfaces. 13 (11) (2021) 13781–13791, https://doi.org/10.1021/acsami.0c22080.

[25] W. Le Zhu, S. Yang, B.F. Ju, J. Jiang, A. Sun, Scanning tunneling microscopy-based on-machine measurement for diamond fly cutting of micro-structured surfaces, Precis. Eng. 43 (2016) 308–314, https://doi.org/10.1016/j.precisioneng.2015.08.011.

[26] J. Jiang, T. Luo, G. Zhang, Y. Dai, Novel tool offset fly cutting straight-groove-type micro structure arrays, J. Mater. Process. Technol. 288 (2021) 116900.

[27] H. Lu, D. Lee, J. Kim, S. Kim, Modeling and machining evaluation of microstructure fabrication by fast tool servo-based diamond machining, Precis. Eng. 38 (1) (2014) 212–216, https://doi.org/10.1016/j.precisioneng.2013.06.004.

[28] Z. Zhu, S. To, S. Zhang, Theoretical and experimental investigation on the novel end-fly-cutting-servo diamond machining of hierarchical micro-nanostructures, Int. J. Mach. Tools Manuf. 94 (2015) 15–25, https://doi.org/10.1016/j.ijmachtools.2015.04.002.

[29] S.J. Zhang, S. To, Z.W. Zhu, G.Q. Zhang, A review of fly cutting applied to surface generation in ultra-precision machining, Int. J. Mach. Tools Manuf. 103 (2016) 13–27, https://doi.org/10.1016/j.ijmachtools.2016.01.001.

[30] A.Y. Yi, L. Li, Design and fabrication of a microlens array by use of a slow tool servo, Opt. Lett. 30 (13) (2005) 1707.

[31] W. Le Zhu, F. Duan, X. Zhang, Z. Zhu, B.F. Ju, A new diamond machining approach for extendable fabrication of micro-freeform lens array, Int. J. Mach. Tools Manuf. 124 (2018) 134–148, https://doi.org/10.1016/j.ijmachtools.2017.10.007.

[32] Y. Yuan, D. Zhang, X. Jing, H. Zhu, W. Le Zhu, J. Cao, K.F. Ehmann, Fabrication of hierarchical freeform surfaces by 2D compliant vibration-assisted cutting, Int. J. Mech. Sci. 152 (2019) 454–464, https://doi.org/10.1016/J.IJMECSCI.2018.12.051.

[33] G. Yan, F. Fang, Fabrication of optical freeform molds using slow tool servo with wheel normal grinding, CIRP Ann. 68 (1) (2019) 341–344.

[34] M. Mukaida, J. Yan, Fabrication of hexagonal microlens arrays on single-crystal silicon using the tool-servo driven segment turning method, Micromachines. 8 (11) (2017) 323, https://doi.org/10.3390/mi8110323.

[35] Y.M. Song, Y. Xie, V. Malyarchuk, J. Xiao, I. Jung, K.-J. Choi, Z. Liu, H. Park, C. Lu, R.-H. Kim, R. Li, K.B. Crozier, Y. Huang, J.A. Rogers, Digital cameras with designs inspired by the arthropod eye, Nature 497 (7447) (2013) 95–99, https://doi.org/10.1038/nature12083.

[36] Y. Zhang, M. Cui, X. Fan, B. Zhang, W. Wang, The fabrication and fast replication of out of plane parabolic microlens arrays, Sensors Actuators A Phys. 216 (2014) 190–195, https://doi.org/10.1016/J.SNA.2014.04.021.

[37] T. Zhang, P. Li, H. Yu, F. Wang, X. Wang, T. Yang, W. Yang, W.J. Li, Y. Wang, L. Liu, Fabrication of flexible microlens arrays for parallel super-resolution imaging, Appl. Surf. Sci. 504 (2020) 144375.

[38] J.-W. Pan, C.-M. Wang, H.-C. Lan, W.-S. Sun, J.-Y. Chang, Homogenized LED-illumination using microlens arrays for a pocket-sized projector, Opt. Express. 15 (17) (2007) 10483.

[39] G. Chu, F. Chen, B. Zhao, X. Zhang, E. Zussman, O.J. Rojas, Self-Assembled Nanorods and Microspheres for Functional Photonics: Retroreflector Meets Microlens Array, Adv. Opt. Mater. 9 (9) (2021) 2002258, https://doi.org/10.1002/adom.202002258.

[40] Y. Li, Y. Liu, D. Luo, A photo-switchable and photo-tunable microlens based on chiral liquid crystals, J. Mater. Chem. C. 7 (48) (2019) 15166–15170.

[41] S. Masuda, S. Takahashi, T. Nose, S. Sato, H. Ito, Liquid-crystal microlens with a beam-steering function, Appl. Opt. 36 (20) (1997) 4772, https://doi.org/10.1364/AO.36.004772.

[42] A. Akatay, C. Ataman, H. Urey, High-resolution beam steering using microlens arrays, Opt. Lett. 31 (19) (2006) 2861.

[43] I.B. Sohn, H.K. Choi, Y.C. Noh, J. Kim, M.S. Ahsan, Laser assisted fabrication of micro-lens array and characterization of their beam shaping property, Appl. Surf. Sci. 479 (2019) 375–385, https://doi.org/10.1016/J.APSUSC.2019.02.083.

[44] Y.L. Chen, Z. Li, F. Chen, H. Lin, B.F. Ju, Y. Liu, Development of an Optimized Three-Axis Fast Tool Servo for Ultraprecision Cutting, IEEE/ASME Trans. Mechatron. (2021) 1–11, https://doi.org/10.1109/TMECH.2021.3109696.

[45] X.u. Yang, W.-L. Zhu, Design, Analysis, and Test of a Novel Self-Sensing Fast Tool Servo, IEEE Trans. Ind. Inform. 16 (7) (2020) 4447–4455, https://doi.org/10.1109/TII.2019.2945360.

[46] H. Du, W. Yip, Z. Zhu, S. To, Development of a two-degree-of-freedom vibration generator for fabricating optical microstructure arrays, Opt. Express. 29 (16) (2021) 25903, https://doi.org/10.1364/OE.433720.

[47] H. Du, S. To, T. Yin, Z. Zhu, Microstructured surface generation and cutting force prediction of pure titanium TA2, Precis. Eng. 75 (2022) 101–110, https://doi.org/10.1016/J.PRECISIONENG.2022.02.004.

[48] J. Long, P. Fan, M. Zhong, H. Zhang, Y. Xie, C. Lin, Superhydrophobic and colorful copper surfaces fabricated by picosecond laser induced periodic nanostructures, Appl. Surf. Sci. 311 (2014) 461–467, https://doi.org/10.1016/J.APSUSC.2014.05.090.

[49] W. Wang, D. Rosenmann, D.A. Czaplewski, X. Yang, J. Gao, Realizing structural color generation with aluminum plasmonic V-groove metasurfaces, Opt. Express. 25 (2017) 20454–20465, https://doi.org/10.1364/OE.25.020454.

[50] C.-Y. Peng, C.-W. Hsu, C.-W. Li, P.-L. Wang, C.-C. Jeng, C.-C. Chang, G.-J. Wang, Flexible Photonic Crystal Material for Multiple Anticounterfeiting Applications, ACS Appl. Mater. Interfaces. 10 (11) (2018) 9858–9864, https://doi.org/10.1021/acsami.8b00292.

[51] Y. He, T. Zhou, X. Dong, P. Liu, W. Zhao, X. Wang, Y. Hu, J. Yan, Generation of high-saturation two-level iridescent structures by vibration-assisted fly cutting, Mater. Des. 193 (2020) 108839, https://doi.org/10.1016/j.matdes.2020.108839.